PAPER

Divertor map with freedom of geometry and safety factor profile

View the article online for updates and enhancements.

Divertor map with freedom of geometry and safety factor profile

T Kroetz[1,5]**, M Roberto**[2]**, I L Caldas**[1] **and R L Viana**[3] **and P J Morrison**[4]

[1] Instituto de Física, Universidade de São Paulo, 05315-970, São Paulo, São Paulo, Brazil

[2] Instituto Tecnológico de Aeronáutica, Centro Técnico Aeroespacial, Departamento de Física, 12228-900, São José dos Campos, São Paulo, Brazil

[3] Departamento de Física, Universidade Federal do Paraná, 81531-990, Curitiba, Paraná, Brazil

[4] Department of Physics and Institute for Fusion Studies, University of Texas, Austin, TX 78712-1060, USA

E-mail: viana@fisica.ufpr.br

Abstract

An explicit, area-preserving and integrable magnetic field line map for a single-null divertor tokamak is obtained using a trajectory integration method to represent equilibrium magnetic surfaces. The magnetic surfaces obtained from the map are capable of fitting different geometries with freely specified position of the X-point, by varying free model parameters. The safety factor profile of the map is independent of the geometric parameters and can also be chosen arbitrarily. The divertor integrable map is composed of a nonintegrable map that simulates the effect of external symmetry-breaking resonances, so as to generate a chaotic region near the separatrix passing through the X-point. The composed field line map is used to analyze escape patterns (the connection length distribution and magnetic footprints on the divertor plate) for two equilibrium configurations with different magnetic shear profiles at the plasma edge.

(Some figures may appear in colour only in the online journal)

1. Introduction

It is well known that tokamak equilibria have magnetic field lines that lie on nested isobaric toroidal surfaces called *magnetic surfaces* [1], and that the cross-sectional shape of these magnetic surfaces plays an important role in determining plasma stability and confinement. Of interest here are divertor tokamaks that possess equilibria with an ideal (integrable) separatrix with one or two X-points that separates the closed from open magnetic surfaces. The separatrix defines the plasma border and diverts particles that escape from the plasma to divertor plates [2].

External and internal resonances between the equilibrium and perturbation magnetic fields break the ideal separatrix, replacing it with a homoclinic tangle, and a resulting layer of chaotic magnetic field lines that are by design guided to the divertor collector plates [3, 4]. The escaping ions recombine at the plates and form a neutral gas that can be pumped away from the tokamak (reactor) core.

---

[3] Permanent address: Departamento de Fisica, Universidade Tecnologica Federal do Parana, 85505-390, Pato Branco, Parana, Brazil.

The X-points are formed when the magnetic field resulting from external coils and the associated plasma response create points of null poloidal magnetic field. A single-null configuration has only one X-point, from which emanate separatrix branches delimiting three different regions of the tokamak vessel (cf figure 1). The plasma region is located in the larger lobe of the separatrix above the X-point, while another private flux region is located in a lobe below the X-point. A region of external magnetic surfaces (or open surfaces) surrounds both lobes. The external private flux magnetic surfaces and external surfaces intercept the collector plates and the corresponding magnetic field lines guide the escaping plasma to this region which is designed to accept a high-energy flux.

The divertor of ITER is designed to withstand a heat load of 5–10 MW m^{-2} that is expected to come from alpha particles resulting from fusion reactions taking place in the plasma core [5]. The equilibrium description of magnetic surfaces is obtained from large computer codes based on numerical solutions of the Grad–Shafranov equation [6, 7]. This methodology, although necessary for designing divertor geometries tailored to specific needs, may be too heavy for
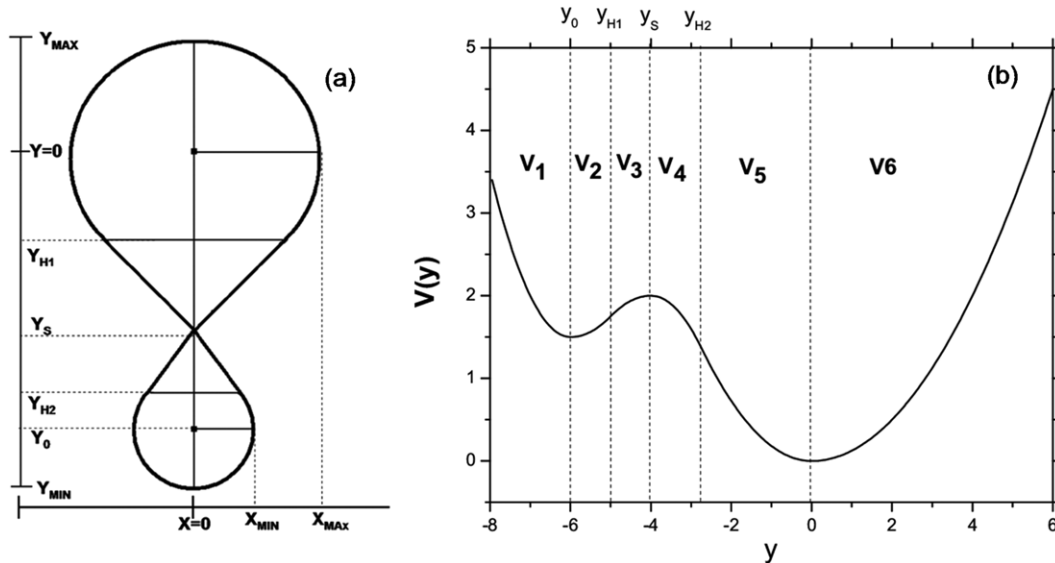
Figure 1. (*a*) Schematic view of a separatrix in rectangular coordinates indicating the meaning of each geometric parameter related to $V(y)$ for a single-null divertor configuration. (*b*) The potential function $V(y)$ for the geometric parameters $x_{MAX} = 2$, $y_{MIN} = 1$; $y_{MIN} = -7$; $y_{MAX} = 4$; $y_{H1} = -5$; $y_{H2} = -2.75$; $y_S = -4$; $y_0 = -6$.

studying some basic phenomena of field line dynamics near the separatrix, such as chaotic transport. For such basic phenomena it is often preferable to use magnetic field line maps, which are much faster to compute yet still retain the basic features one is looking for in studying divertor geometries.

Magnetic field line maps are sets of equations that provide the coordinates of a magnetic field line at a fixed toroidal angle. Given the coordinates of a field line in such a poloidal plane, the map gives the coordinates after the field line has traversed the torus one time the long way around. The principal advantage of using field line maps is the assurance of the symplectic character of the system, the *sine qua non* requisite of Hamiltonian systems.

Previously magnetic field line maps have been used to investigate phenomenological aspects of field line trajectories and pattern deposition in divertor configurations. Some of these maps have been obtained directly from the magnetic field equations [8–10] by means of a procedure that uses generalized Poincaré integrals [11]. Other divertor maps have been obtained by the mathematical construction of appropriate generating functions and canonical transformations [12–16]. Divertor maps using the geometry of the DIII-D tokamak have been obtained by fitting experimental data to find appropriate expressions for equilibrium Hamiltonians [17–19].

However, it may happen that the discretization procedure used for obtaining field line maps from corresponding magnetic field line equations results in a nonphysical perturbation that is proportional to the discretization parameter. Hence, systematic procedures for obtaining field line maps from field line equations that preserve the symplectic property are important tools. The symplectic property is particularly important for studies of long 'time' (many toroidal transits) transport, when extremely long orbits have to be considered. A similar situation occurs in celestial mechanical numerical studies of N-body problems using symplectic integrators.

We have recently proposed [22] the use of a general method (the trajectory integration method of [23]) for obtaining integrable symplectic field line maps with specified fixed points and separatrices. For the single-null divertor of [22], the fixed point was a single X-point placed between the plasma boundary and the divertor plates, as described above and in figure 1. We used this method to obtain an integrable field line map compatible with the single null, and then obtained a nonintegrable map by adding a perturbation that describes an 'ergodic' limiter. The map obtained in [22] for a single-null divertor was based on a specific equilibrium plasma configuration with little freedom to choose different configurations.

In this paper we apply the trajectory integration method to obtain a symplectic field line map with adjustable parameters for describing a variety of plasma equilibrium configurations with a divertor. This procedure increases the complexity of the equations but allows for tailoring the map to different configurations, which is desirable when considering distinct separatrix (and consequently internal and external surfaces) divertor geometries. The safety factor associated with each surface can also be chosen independently of the geometry of the configuration adopted. This feature makes possible a variety of studies; for example, the study of the influence of the elongation of configurations or altering of safety factor profiles on chaotic layer formation and deposition patterns of magnetic field lines at collector plates.

Previous works proposed discrete divertor maps with varying elongation [20] and average shear [21]. However, in these works these two characteristics cannot be varied independently. In contrast, the trajectory integration method provides integrable divertor maps for which these features can be varied independently. Another advantage of the map we obtain, in addition to the geometry and safety factor versatility, is the assurance of the symplectic character. Moreover, having a field line map that conveniently describes

integrable equilibrium magnetic configurations, we can then add other perturbations in an independent way in order to create nonintegrable divertor maps.

The rest of the paper is organized as follows: in section 2 we outline the basics of the trajectory integration method and show how it can be applied to obtain a map for a single-null divertor configuration with many free parameters. Section 3 discusses the equilibrium magnetic field model used to obtain a desired safety factor profile. Section 4 shows the effect of adding a symmetry-breaking perturbation that destroys integrability and allows for the existence of chaotic field lines. Finally, section 5 is devoted to our conclusions.

2. Trajectory integration method

Now we describe the trajectory integration method, a versatile and reliable method for obtaining symplectic field line maps for configurations where desired fixed points are specified [22, 23]. Then, by direct application of this method we construct our divertor map, a map that possesses the freedom to specify a single or double-null point as needed in order to design suitable divertor devices.

2.1. The method

The magnetic field line behavior in a toroidal plasma device like a tokamak, in an equilibrium state, is known to be described by a single degree-of-freedom Hamiltonian system, in which the canonically coordinate variables are the coordinates (or, more properly, suitable functions of these coordinates) of the field line intersection with a given poloidal surface of section [37]. The time-like coordinate is thus the toroidal angle that parametrizes the field line equations. Note, when the state being described is an equilibrium state, the physical time does not explicitly appear. Hence, the field line description has to be taken in the Lagrangian sense, and no time-dependence whatsoever is meant. Internal or external perturbations that break the toroidal symmetry introduce a dependence on the toroidal coordinate that spoils integrability and allows for the existence of chaotic field lines.

The basic idea of the trajectory integration method is to exploit similarities between the Hamiltonian dynamics describing the field line behavior and the one-dimensional motion of a particle under a suitably chosen potential function (in the latter case we obviously mean the physical time, rather than a parametrization). The equilibrium points are the extrema of the potential function, and we can tailor the potential function to meet the desired fixed points of the field line map.

The trajectory integration method can be summarized in three steps (see [22, 23] for further details):

(1) Choose an adequate expression $V(y)$ in a Hamiltonian denoted by Ψ,

$$\Psi(x, y) = \frac{x^2}{2} + V(y), \qquad (1)$$

with extremum points located at desired values of y. These positions will correspond to the elliptic (O-points)

and hyperbolic (X-points) fixed points in the phase space with coordinates (x, y). The equilibrium Hamiltonian is integrable and $V(y)$ must allow for analytic solutions of the corresponding canonical equations. The potential $V(y)$ is an auxiliary expression used in the method, one that generates closed surfaces of constant Ψ (level sets) with the desired topology of the magnetic surfaces to be represented by the map.

(2) Solve Hamilton's equations,

$$\frac{dy}{dt} = \frac{\partial \Psi}{\partial x}, \qquad \frac{dx}{dt} = -\frac{\partial \Psi}{\partial y}, \qquad (2)$$

and find the continuous solutions $(x(x_i, y_i, t), y(x_i, y_i,t))$, where x_i and y_i are the initial conditions for the solutions. We emphasize that the meaning of t, in the field line map, is a toroidal-like coordinate that parametrizes the field line flow in a Lagrangian sense.

(3) Discretize the continuous solutions by making the transformation

$$(x(x_i, y_i, t), y(x_i, y_i, t))$$
$$\rightarrow (x_{n+1}(x_n, y_n, \Delta), y_{n+1}(x_n, y_n, \Delta)). \qquad (3)$$

The resulting equations comprise the discrete map.

The parameter Δ is related to the rotation of the field line between intersections with the surface of section, after successive applications of the map equations. In an equilibrium plasma this rotation is given by the rotational transform, the inverse of which is usually called the safety factor for stability reasons. Because the topology of the magnetic surfaces and the fixed points of the map are independent of Δ, we can reproduce any desirable safety factor profile by imposing appropriate dependence $\Delta(\Psi)$, independently of the chosen geometry.

The larger the number of regions (and correspondingly the matching points) the more free parameters the equilibrium map has, which offers an unlimited capability for adjusting the geometry of the magnetic surfaces. In this sense, the trajectory integration method allows a high flexibility in the choice of equilibrium parameters.

Although our map describes diverted magnetic fields without toroidal corrections, close to the separatrix $1/x$ is nearly constant, so if we make our layer small enough we get a good approximation for the equilibrium field in large aspect ratio tokamaks.

2.2. Map equations for a single-null divertor

For a single-null divertor the potential function $V(y)$ must have a double-well shape, so as to create curves in phase space with two closed regions delimited by a separatrix, as is the case for single-null divertor configurations. The expression for $V(y)$ will be written as six parabolic branches matching smoothly at specified points, so as to ensure the integrability of Hamilton's equations. The continuous solutions of Hamilton's equations in each region will be oscillatory in t for positive concavity of

$V(y)$ and hyperbolic for regions of negative concavity. The expressions for $V(y)$ in each 'parabolic' region are given by

$$V(y) = \begin{cases} \frac{1}{2}a_1(y - y_0)^2 + b' & y \leqslant y_0 \\ \frac{1}{2}a_2(y - y_0)^2 + b' & y_0 \leqslant y \leqslant y_{H1} \\ -\frac{1}{2}a_3(y - y_s)^2 + b & y_{H1} \leqslant y \leqslant y_s \\ -\frac{1}{2}a_4(y - y_s)^2 + b & y_s \leqslant y \leqslant y_{H2} \\ \frac{1}{2}a_5 y^2 & y_{H2} \leqslant y \leqslant 0 \\ \frac{1}{2}a_6 y^2 & 0 \leqslant y. \end{cases} \quad (4)$$

The continuous trajectories using (4) can be obtained by solving equation (2) in each parabolic region. The internal plasma surfaces will correspond to the solutions for $\Psi \leqslant b$ and $y > y_S$, while the divertor private flux surfaces will correspond to the solutions for $\Psi \leqslant b$ and $y < y_S$. The external surfaces are those that satisfy $\Psi > b$.

After applying the discretization procedure we obtain the following map equations for each region:

- For $y_n < y_0$:

$$x_{n+1} = -(y_n - y_0)\sqrt{a_1}\sin(\sqrt{a_1}\Delta) + x_n\cos(\sqrt{a_1}\Delta), \quad (5)$$

$$y_{n+1} = (y_n - y_0)\cos(\sqrt{a_1}\Delta) + \frac{x_n}{\sqrt{a_1}}\sin(\sqrt{a_1}\Delta) + y_0. \quad (6)$$

- For $y_0 < y_n < y_{H1}$:

$$x_{n+1} = -(y_n - y_0)\sqrt{a_2}\sin(\sqrt{a_2}\Delta) + x_n\cos(\sqrt{a_2}\Delta), \quad (7)$$

$$y_{n+1} = (y_n - y_0)\cos(\sqrt{a_2}\Delta) + \frac{x_n}{\sqrt{a_2}}\sin(\sqrt{a_2}\Delta) + y_0. \quad (8)$$

- For $y_{H1} < y_n < y_S$:

$$x_{n+1} = (y_n - y_S)\sqrt{a_3}\sinh(\sqrt{a_3}\Delta) + x_n\cosh(\sqrt{a_3}\Delta), \quad (9)$$

$$y_{n+1} = (y_n - y_S)\cosh(\sqrt{a_3}\Delta) + \frac{x_n}{\sqrt{a_3}}\sinh(\sqrt{a_3}\Delta) + y_S. \quad (10)$$

- For $y_S < y_n < y_{H2}$:

$$x_{n+1} = (y_n - y_S)\sqrt{a_4}\sinh(\sqrt{a_4}\Delta) + x_n\cosh(\sqrt{a_4}\Delta), \quad (11)$$

$$y_{n+1} = (y_n - y_S)\cosh(\sqrt{a_4}\Delta) + \frac{x_n}{\sqrt{a_4}}\sinh(\sqrt{a_4}\Delta) + y_S. \quad (12)$$

- For $y_{H2} < y_n < 0$:

$$x_{n+1} = -y_n\sqrt{a_5}\sin(\sqrt{a_5}\Delta) + x_n\cos(\sqrt{a_5}\Delta), \quad (13)$$

$$y_{n+1} = y_n\cos(\sqrt{a_5}\Delta) + \frac{x_n}{\sqrt{a_5}}\sin(\sqrt{a_5}\Delta). \quad (14)$$

- For $y_n > 0$:

$$x_{n+1} = -y_n\sqrt{a_6}\sin(\sqrt{a_6}\Delta) + x_n\cos(\sqrt{a_6}\Delta), \quad (15)$$

$$y_{n+1} = y_n\cos(\sqrt{a_6}\Delta) + \frac{x_n}{\sqrt{a_6}}\sin(\sqrt{a_6}\Delta). \quad (16)$$

The map defined by equations (5)–(16) will trace out ellipses in the phase space joined smoothly with the hyperbolas defined by map equations (9)–(12). For our purposes, we will relate the parameters in the above expressions to geometric parameters that describe the separatrix formed in phase space by the solution of Hamilton's equations.

The geometric parameters chosen to fit a particular design are the following: x_{MAX}, x_{MIN}, y_{MAX}, y_{MIN}, y_0, y_{H1}, y_{H2} and y_S. The meaning of each one of these parameters can be observed in figure 1(*a*). The hyperbolic solutions at $\Psi = \Psi_S$, where Ψ_S is the value of the Hamiltonian at the separatrix (given by b), will trace out straight line segments connecting the X-point to the ellipses formed by the oscillatory solutions. On controlling the values of y_{H1} and y_{H2} we can determine the size of the region where the separatrix can be approximated by straight line segments.

The relationships between the geometric parameters of the separatrix and the analytic parameters in the equations defining $V(y)$ can be found from the requirement that the value of Ψ_S be constant at any point on the separatrix. This is a particular situation, for Ψ is constant on any magnetic surface. The matching relations at each point separating the parabolic regions are the continuity of $V(y)$ and its first derivative.

The relations obtained through this procedure are

$$b = \frac{x_{MAX}^2}{2}, \qquad b' = \frac{x_{MAX}^2}{2} - \frac{x_{MIN}^2}{2}, \quad (17)$$

$$a_1 = \frac{x_{MIN}^2}{(y_{MIN} - y_0)^2}, \qquad a_2 = \frac{x_{MIN}^2}{(y_{H1} - y_0)(y_S - y_0)}, \quad (18)$$

$$a_3 = \frac{-x_{MIN}^2}{[(y_{H1} - y_0)(y_{H1} - y_S) - (y_{H1} - y_S)^2]}, \quad (19)$$

$$a_4 = \frac{x_{MAX}^2}{(y_{H2} - y_S)^2 - y_{H2}(y_{H2} - y_S)}, \qquad a_5 = \frac{x_{MAX}^2}{y_{H2}y_S},$$

$$a_6 = \frac{x_{MAX}^2}{y_{MAX}^2}. \quad (20)$$

In figure 1(*b*) we depict the graph of the potential function $V(y)$ for a given set of geometric parameter values with the six parabolic regions. The figure also shows the connection points y_0, y_{H1}, y_S, y_{H2} delimiting the parabolic regions of $V(y)$.

Although equations (5)–(16) result from the discretization of continuous solutions for each region, these equations are not able to map a point from a specific region of $V(y)$ to another. For example, we cannot use equations (11) and (12) to map the point (in the surface of section) of coordinates (x_n, y_n) into the next point (x_{n+1}, y_{n+1}), if $y_n < y_{H2} < y_{n+1}$. The map equations to be used should be equations (13) and (14) instead, at the exact 'time' marking the transition from the parabolic region 4 to region 5.

It remains to gather two pieces of information to finish this transformation. The first is the abscissa x_{H2} of the connection point between regions 4 and 5. The second is the time interval t_{H2} (in terms of the parameter Δ) spent to take (x_n, y_n) into (x_{H_2}, y_{H2}). After incorporating this information we can use the map equations (13)–(14), during the time interval $(\Delta - t_{H2})$, necessary to transform the point (x_{H_2}, y_{H2}) into the point (x_{n+1}, y_{n+1}). Finally, the connection point coordinates

(x_{H2}, y_{H2}) are given by the continuous version of equations (11) and (12) at $t = t_{H2}$, according to

$$x_{H2} = (y_n - y_S)\sqrt{a_4}\sinh(\sqrt{a_4}t_{H2}) + x_n\cosh(\sqrt{a_4}t_{H2}), \quad (21)$$

$$y_{H2} = (y_n - y_S)\cosh(\sqrt{a_4}t_{H2}) + \frac{x_n}{\sqrt{a_4}}\sinh(\sqrt{a_4}t_{H2}) + y_S. \quad (22)$$

Equating the field line Hamiltonian at (x_n, y_n) and at the connection point (x_{H2}, y_{H2}) we find

$$x_{H2} = [x_n^2 - a_4(y_n - y_S)^2 - a_5 y_{H2}^2 + 2b]^{1/2}. \quad (23)$$

Substituting equation (21) into (22) to eliminate the sinh term, there results an expression for t_{H2}, namely

$$t_{H2} = \frac{1}{\sqrt{a_4}}\cosh^{-1}\left[\frac{x_{H2}x_n - a_4(y_n - y_S)(y_{H2} - x_S)}{x_n^2 - a_4(y_n - y_S)^2}\right]. \quad (24)$$

Therefore, the point (x_{n+1}, y_{n+1}) must be defined as follows:

$$x_{n+1} = -y_{H2}\sqrt{a_5}\sin(\sqrt{a_5}(\Delta - t_{H2}))$$
$$+ x_{H2}\cos(\sqrt{a_5}(\Delta - t_{H2})), \quad (25)$$

$$y_{n+1} = y_{H2}\cos(\sqrt{a_5}(\Delta - t_{H2}))$$
$$+ \frac{x_{H2}}{\sqrt{a_5}}\sin(\sqrt{a_5}(\Delta - t_{H2})), \quad (26)$$

which are equations that describe the transition from the parabolic region 4 to 5.

This connection procedure must be applied for each matching point at the boundaries of the parabolic regions. Since the expression for $V(y)$ of (4) has five such connection points, each one will need two transition maps (since we will have two crossing directions). Thus, the complete integrable map will be composed of sixteen parts. The explicit map equations are rather involved, although they contain only elementary functions. The complete set of map equations for each matching point is given in appendix A. The symplectic property for the portions of the map that are 'region preserving' as well the portions of the map that affect the transitions between regions are automatically fulfilled, since Δ depends only on Ψ, as was demonstrated explicitly in [22]. Furthermore, the map can be inverted by changing the x and t variables and considering negative Δ-values in the map between regions.

Sample equilibrium magnetic surfaces obtained from the complete set of map equations are shown in figure 2 for the following parameters: $x_{MAX} = 2$, $y_{MIN} = 1$, $y_{MIN} = -7$, $y_{MAX} = 4$, $y_{H1} = -5$, $y_{H2} = -2.75$, $y_S = -4$ and $y_0 = -6$. As the general geometric properties of the magnetic surfaces do not depend on the values chosen for Δ, we are able to set $\Delta = 1$ for all surfaces. The figure shows three different kinds of surfaces: (i) the plasma magnetic surfaces (in black); (ii) the divertor private flux surfaces (in red) and (iii) the external surfaces (in green). Moreover we show in figure 2 a reference surface for Ψ_{95} (in blue) where $\Psi = 95\%\Psi_S$.

The effects of changing various geometrical parameters describing the equilibrium state are illustrated in figure 3, where four cases with values different from those considered in figure 2 are shown. Decreasing x_{MAX} from 2 (as in figure 2)
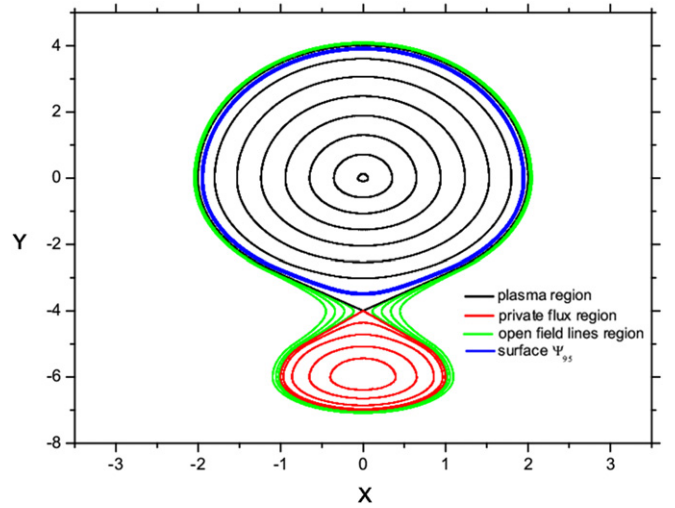

Figure 2. Equilibrium magnetic surfaces obtained from the single-null divertor map (see appendix A for the equations) with the same geometric parameters as in figure 1(*b*). The surfaces in black are in the plasma region. We depict in blue a reference magnetic surface for which $\Psi = 95\%\Psi_S$. The external surfaces and the divertor private flux surfaces are depicted in green and red, respectively.

to 1.5 yields an elongation, a stretching of the whole set of plasma magnetic surfaces along the y-direction (cf figure 3(*a*)). Increasing y_{MAX} from 1 to 5 produces a stretching along the y-direction that is less pronounced near the null point (cf figure 3(*d*)). On changing y_{H2} and y_S similar stretching occurs, but along the x-direction (cf figures 3(*b*) and (*c*), respectively). The variety of shapes we obtain from changing these free equilibrium parameters demonstrates the versatility of the field line map obtained by using our method.

3. Equilibrium magnetic field model

The Hamilton system with the Hamiltonian of equation (1) has invariant curves in its phase space that are the magnetic surfaces we want to obtain from the field line map. When the continuous time t is replaced by the discretization parameter Δ with a dependence on Ψ, the resulting map no longer represents solutions to the Hamiltonian system from which it was originally derived. Rather, the invariant curves (in the surface of section) obtained from the map have safety factors generally different from the original continuous system. In fact, the safety factor profile can be chosen arbitrarily by specifying the function $\Delta(\Psi)$ without affecting the topology adopted for the magnetic surfaces. If one wishes to model a known equilibrium state with a known winding number profile (inverse of the safety factor) then one can input this information into the map model.

If we adopt $\Delta = 1$ for all values of Ψ, then the map has a safety factor profile identical to that of the original continuous system. However, if we choose $\Delta(\Psi)$ to match our known equilibrium, then it turns out that a convenient representation is given by the following:

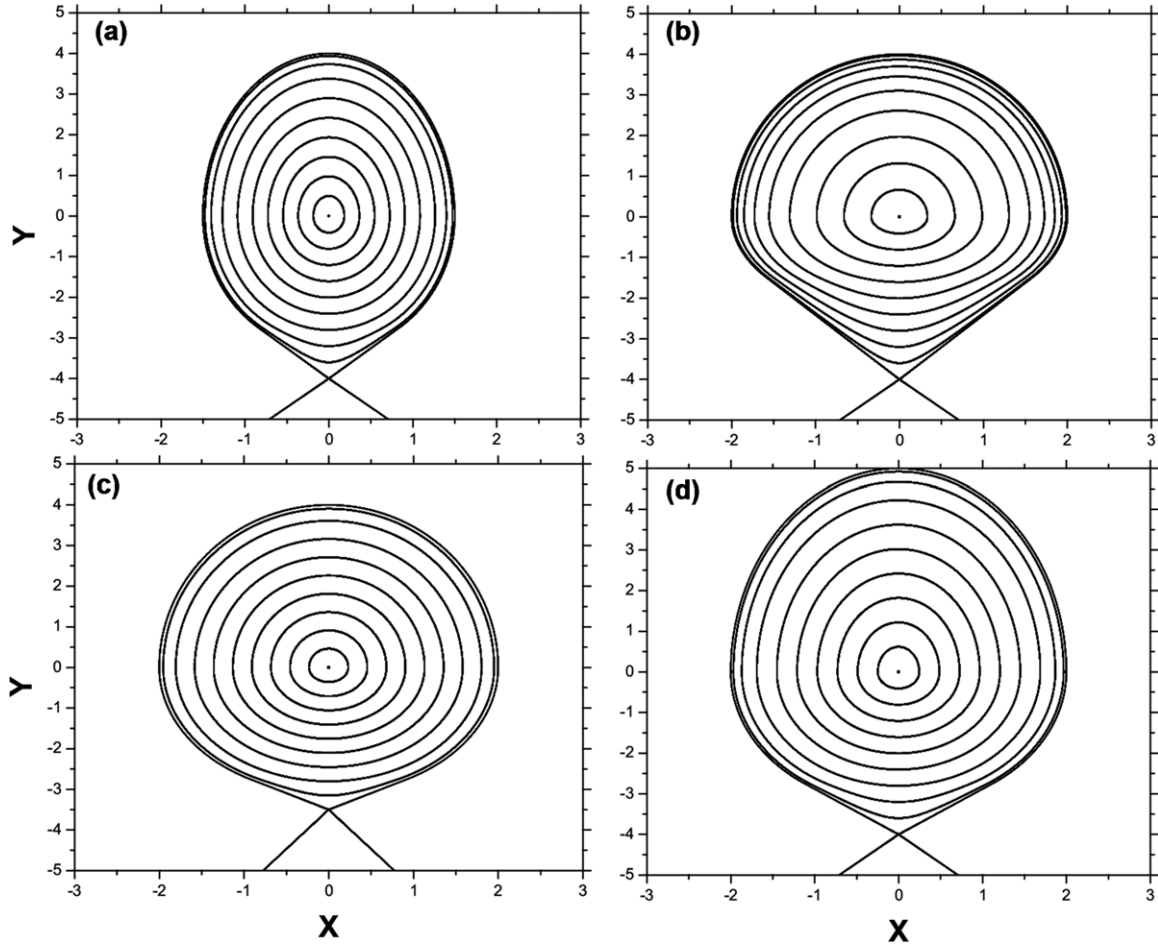$$\Delta = \frac{T(\Psi)}{q(\Psi)}, \quad (27)$$

Figure 3. Equilibrium magnetic surfaces obtained with (*a*) $x_{\mathrm{MAX}} = 1.5$; (*b*) $y_{\mathrm{H2}} = 1.5$, (*c*) $y_{\mathrm{S}} = 3.5$ and (*d*) $y_{\mathrm{MAX}} = 5$. The other geometric parameters are the same as in figure 1(*b*).

where $T(\Psi)$ is the rotation period of the invariant curves Ψ associated with the continuous system and $q(\Psi)$ is the safety factor of the magnetic surface we intend to represent by the invariant curve Ψ.

The function $T(\Psi)$ can be found by computing the time spent by the continuous trajectory in each region of $V(y)$ using a procedure similar to that explained in section 2, where, e.g., we found the time t_{H2} in equation (24). Doing this we obtain an analytical expression for the rotation period associated with the surfaces. There are different expressions depending on the range of values of Ψ. The analytic expressions for all possible cases (closed plasma surfaces, divertor private surfaces and external surfaces) are explicitly written in appendix B.

Given the function $T(\Psi)$, any desired safety factor profile $q(\Psi)$ can be obtained using equation (27), thereby representing different equilibrium configurations with a variety of free parameters. In principle, it is not even necessary to assign a functional form of $q(\Psi)$, since it suffices to specify a set of values of $q(\Psi)$ at given points in the tokamak vessel.

In the following we will consider a specific model with a monotonic safety factor profile and a singularity at $\Psi = \Psi_{\mathrm{S}}$. The particular expression for $q(\Psi)$ with these features is polynomial for $0 \leqslant \Psi < \Psi_{95}$ and logarithmic for

$\Psi_{95} < \Psi \leqslant \Psi_{\mathrm{S}}$, i.e.

$$q(\Psi) = \begin{cases} q_0 + c_1\Psi + c_2\Psi^2, & \Psi \leqslant \Psi_{95} \\ \alpha\ln(\Psi_{\mathrm{S}} - \Psi) + \beta, & \Psi_{95} \leqslant \Psi. \end{cases} \quad (28)$$

In the external region ($\Psi > \Psi_{\mathrm{S}}$) we suppose that the model is symmetric with respect to $\Psi = \Psi_{\mathrm{S}}$. In other words $q(\Psi) = \alpha\ln(\Psi - \Psi_{\mathrm{S}}) + \beta$, for $\Psi > \Psi_{\mathrm{S}}$.

We choose the following free parameters: $q_0 = q(\Psi = 0)$, q_{95} and q'_{95}, where q_{95} is the safety factor value at Ψ_{95} and q'_{95} its derivative with respect to Ψ taken at $\Psi = \Psi_{95}$. The latter is related to the magnetic shear for the reference surface by

$$\hat{s}_{95} = \frac{r_{95}}{q_{95}}\left.\frac{\mathrm{d}q}{\mathrm{d}r}\right|_{r_{95}}, \quad (29)$$

where $r_{95} = \sqrt{2\Psi_{95}}$ is the midplane minor radius of the magnetic surface labeled by Ψ_{95}. The relation between the magnetic shear and the safety factor derivative is thus

$$q'_{95} = \frac{q_{95}\hat{s}_{95}}{2\Psi_{95}}. \quad (30)$$

The constants appearing in the equilibrium model given by equation (28) are related to the physical free parameters
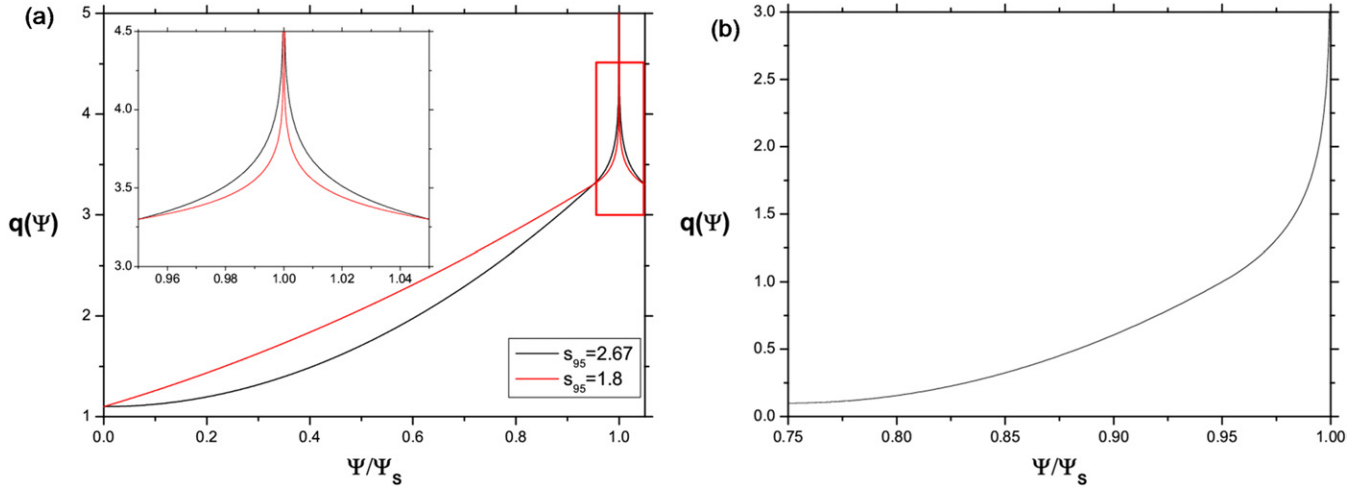
6

Figure 4. (*a*) Radial safety factor profile for the equilibrium model of equation (28) for the plasma core ($\Psi < \Psi_S$) and external regions ($\Psi > \Psi_S$), for $q(0) = 1.1$, $q_{95} = 3.3$, and $\hat{s}_{95} = 1.8$ (red/gray curve) and $\hat{s}_{95} = 2.67$ (black curve). The inset is a magnification of the region surrounding the separatrix surface Ψ_S. (*b*) Radial safety factor profile for the model of equation (28) for the divertor region surfaces, where $q(\Psi = b') = 0.1$ and $q(0.95\Psi_S) = 1$.

above by the following expressions:

$$c_1 = \frac{2(q_{95} - q_0) - q'_{95}\Psi_{95}}{\Psi_{95}}, \qquad (31)$$

$$c_2 = \frac{q_0 - q_{95} + q'_{95}\Psi_{95}}{\Psi_{95}^2}, \qquad (32)$$

$$\alpha = q'_{95}(\Psi_{95} - \Psi_S), \qquad (33)$$

$$\beta = q'_{95} + q'_{95}(\Psi_{95} - \Psi_S)\ln(\Psi_S - \Psi_{95}). \qquad (34)$$

Figure 4(*a*) depicts two radial safety factor profiles, both using $q_0 = 1.1$ and $q_{95} = 3.3$, but with different shear parameter values at Ψ_{95}. Both curves increase monotonically from 1.0 (at the magnetic axis) to 5.0 (at the separatrix Ψ_S), but the smaller shear case ($\hat{s}_{95} = 1.8$, depicted in black) has a slower ascent, whereas the larger shear ($\hat{s}_{95} = 2.67$, depicted in red/gray) provides a steeper increase. However, near the separatrix the slopes are different, as illustrated in the inset of figure 4(*a*). This freedom of parameter choice is highly desirable for fitting the model to the specific needs of a given equilibrium configuration.

The safety factor profile for the divertor private flux region has the same expression as that of (28), where we fix $\hat{s}_{95} = 2$, $q_{95} = 1$ and $q(\Psi = b') = 0.1$ the safety factor at the center of the lower lobe. This profile is shown in figure 4(*b*).

4. Magnetic field line escape due to an ergodic limiter

The concept of an ideal separatrix acting as a barrier that separates the hot plasma from the tokamak chamber first wall is an ideal scenario. Real discharges always have unavoidable resonant perturbations. These resonances can be inherent to the plasma dynamics [24–26], be the result of error fields (asymmetries of the coil alignment) [27, 28], or be intentionally caused by external conductors in order to control plasma instabilities [29, 30]. Generally speaking, the effect of such

perturbations is to replace the ideal equilibrium separatrix by a layer of chaotic magnetic field lines near the plasma border.

Magnetic field lines in this chaotic layer can escape from the confined plasma and eventually reach the divertor plates carrying particles with them. To show how the divertor map can be used to study the field line dynamics of such a chaotic layer, here we simulate the effect of an ergodic limiter, which is an arrangement of currents external to the plasma creating a perturbing magnetic field that is strong in the vicinity of the tokamak wall [31]. Ergodic limiters consists of a set of filamentary conductors carrying electric currents in opposite toroidal directions [32], in such a way that the contribution of the poloidal component of the conductors is negligible. The relevant currents are located at a specific toroidal position and occupy a thin toroidal section.

If the ergodic limiter is composed of *m* pairs of toroidally aligned conductors, then the resulting magnetic field resonates with the equilibrium field lines lying on magnetic surfaces with rational safety factor $q = m/n$, where *m* and *n* are positive integers. Thus, the ergodic limiter causes a resonant perturbation concentrated on the toroidal position occupied by the conductor ring. If this ring is narrow enough, the perturbation caused by the ergodic limiter can be approximated by a delta-function kick at the limiter position, acting on the equilibrium field lines so as to generate a nonintegrable field line configuration.

The impulsive character of the resonant perturbation allows us to obtain an analytical expression for the field line map [38, 39]. The total map is a composition of two maps: (i) an integrable divertor map, just like the one we obtained from the trajectory integration method and (ii) a perturbative map representing the effect of the ergodic limiter. Application of the integrable divertor map represents a toroidal turn of a magnetic field line through the tokamak until it reaches the ergodic limiter position. A perturbative map follows that takes the field line through the local ergodic limiter region.
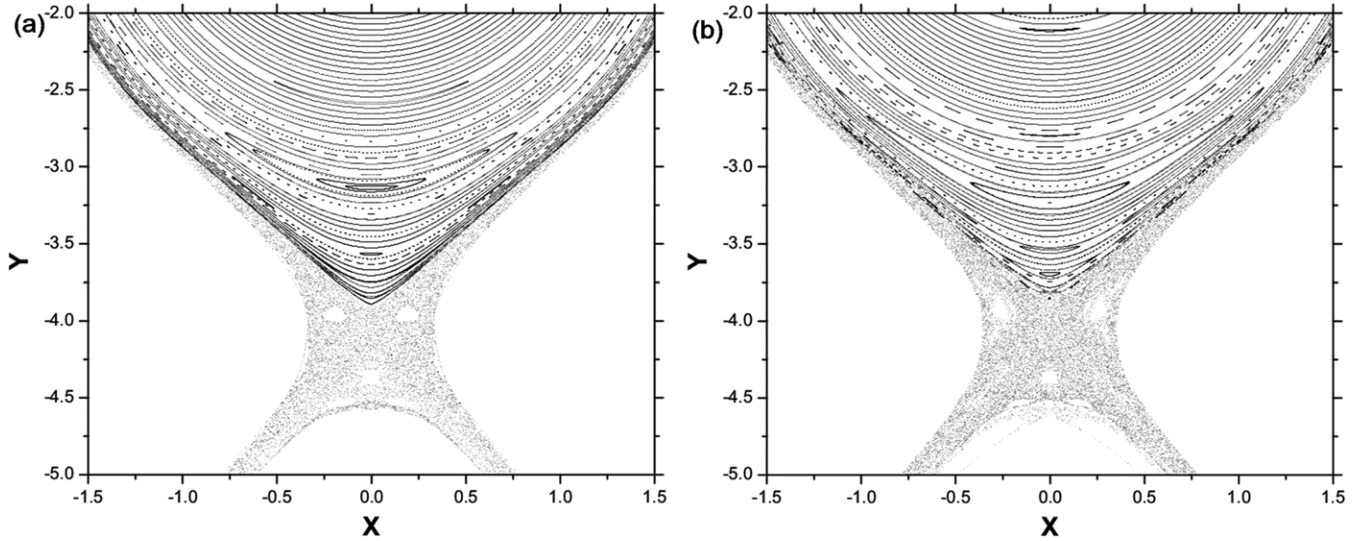
Figure 5. Phase portraits for the total field line map for (*a*) $\hat{s}_{95} = 1.8$ and (*b*) $\hat{s}_{95} = 2.67$. The remaining perturbation parameters are $C = 10^{-2}$ and $m = 3$.

We shall use the perturbative map proposed by Martin and Taylor [33], which identifies the field line intersection with a surface by the local coordinates (ρ, α). The latter are related to the poloidal coordinates (r, θ) in the surface of section through $\rho = r_c - r$ and $\alpha = r_c\theta$, where r_c is the minor radius of the tokamak chamber (which is also the radius of the limiter coil, neglecting the thickness of the vessel).

In the Martin–Taylor model a magnetic field line entering the ergodic limiter at the point (ρ_1, α_1) emerges from it at the point (ρ_2, α_2), where

$$\alpha_2 = \alpha_1 - Ce^{-m\rho_1/r_c}\cos\left(\frac{m\alpha_1}{r_c}\right), \qquad (35)$$

$$\rho_2 = \rho_1 + \frac{r_c}{m}\ln\left[\frac{\cos(m\alpha_2/r_c)}{\cos(m\alpha_1/r_c)}\right] \qquad (36)$$

and the constant C represents the perturbation amplitude that is related to the physical parameters by $C = \mu_0 gm I_h/\pi r_c B_0$ (in SI units). Here μ_0 is the permeability of free space, I_h is the current flowing on the limiter segments and B_0 is the equilibrium toroidal field (supposed to be uniform throughout the vessel).

The total field line map $(x_n, y_n) \rightarrow (x_{n+1}, y_{n+1})$ results from the composition of the integrable divertor map M_D, yielding $(x_n, y_n) \rightarrow (x^*, y^*)$, and the perturbing map M_P, which gives $(x^*, y^*) \rightarrow (x_{n+1}, y_{n+1})$. The iteration of the total map requires a change of the parameter Δ each time the field line emerges from the limiter region, since after the impulsive perturbation a field line jumps to another magnetic surface $\Psi(x_{n+1}, y_{n+1})$ that has a different safety factor. Thus, we apply equation (27) to select a corrected Δ parameter to map the field line through the next toroidal turn.

We present numerical simulations using the following perturbation parameters: $C = 10^{-2}$, $r_c = 5$ and $m = 3$. The phase portraits shown in figure 5 were obtained by considering 55 initial conditions along the line $x = 0$ and in the interval $-4 < y < -2$, and each initial condition was iterated 10^3

times. The equilibrium radial safety factors depicted in figure 4 were used, with the two cases considered therein: low shear as in figure 5(*a*) and high shear as in figure 5(*b*).

A noteworthy aspect of these phase portraits is that, although the initial conditions in both cases were chosen within the plasma region, some chaotic magnetic field lines close to the tokamak border penetrate the region external to the ideal separatrix. Moreover, the equilibrium configuration with larger shear $\hat{s}_{95}$ of figure 5(*b*) presents a slightly wider stochastic layer in comparison with the lower shear case of figure 5(*a*).

The magnetic field line escape is channeled to the divertor plates. Although the chaotic field line region appears to be uniform, chaotic field lines hit the divertor plates in a nonuniform fashion [40]. We investigate this using the total map described above, so as to obtain the position of strike points of escaping magnetic field lines on the divertor plate, as well as the number of toroidal turns performed by the lines before reaching the plate. This gives valuable information on the nonuniform deposition patterns of field lines on the divertor plate. However, we must keep in mind that this is a picture of a specific toroidal position of the field lines, and does not show what occurs between two consecutive intersections with the surface of section.

We choose, rather arbitrarily, to locate the divertor collection plate at the position $y_{H1} = -5$. The point where an escaping field line hits the divertor plate will be labeled (x_F, y_{H1}, ϕ_F). If both of the conditions $y_n > y_{H1}$ and $y* < y_{H1}$ are fulfilled, we consider the field line as hitting the divertor plane between these two iterations.

If this situation is detected, we have to resort to a modification of the iteration procedure to find numerically the position of an escaping field line between two map iterations. Then, we return to the fact that the integrable part of the map was derived by first discretizing the continuous-time field line equations. Hence, we can use the continuous version of equations (9) and (10) to discover the exact final position
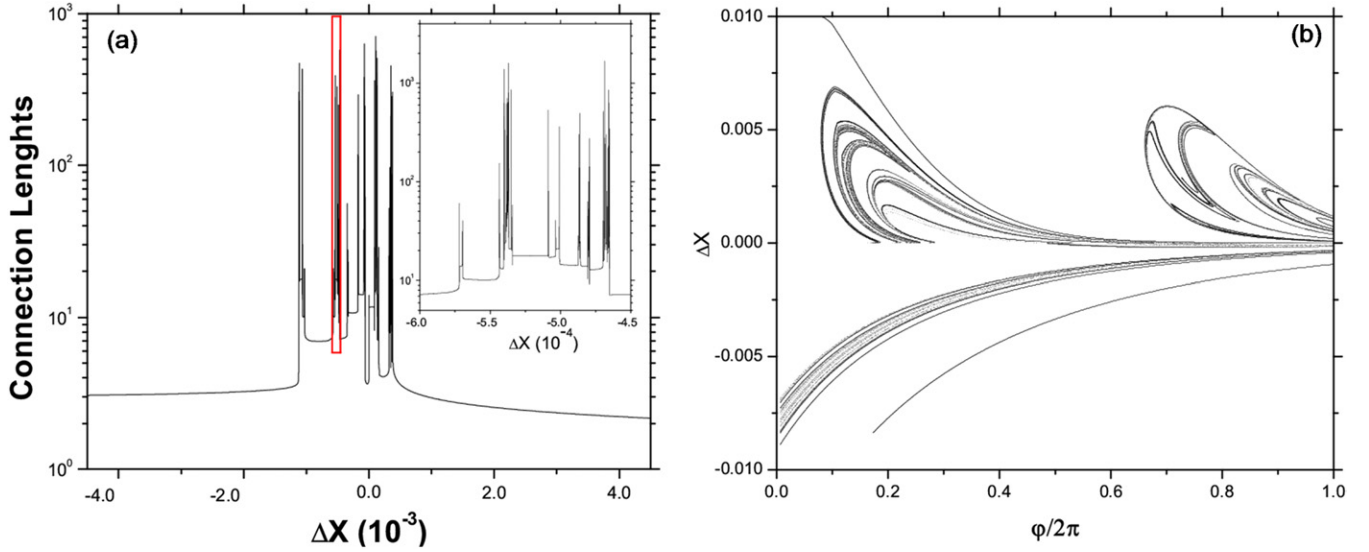
Figure 6. (*a*) Distribution of connection lengths of field lines colliding with the divertor plate for the same parameters as in figure 5(*a*). The inset shows a magnification of the box marked in red/gray. (*b*) Magnetic footprint corresponding to this case.

(x_F, y_{H1}, ϕ_F) of the line, which is

$$x_F = - \left[x_n^2 - a_2 (y_{H1} - y_0)^2 - a_3 (y_n - y_S)^2 + 2(b - b') \right]^{1/2},$$
(37)

$$t_F = \frac{1}{\sqrt{a_3}} \cosh^{-1} \left[\frac{x_F x_n - a_3 (y_n - y_S)(y_{H1} - x_S)}{x_n^2 - a_3 (y_n - y_S)^2} \right],$$
(38)

where b and b' are given by equation (17), and t_F is the time it takes for the field line until it reaches the plate at the final toroidal angle ϕ_F, given by

$$\phi_F = 2\pi \frac{t_F}{\Delta_n},$$
(39)

where $\Delta_n \equiv \Delta(\Psi(x_n, y_n))$.

The number of toroidal turns necessary for the field line to strike the divertor plate is also called its 'connection length' C_L and it is given by

$$C_L = N + \frac{t_F}{\Delta_n},$$
(40)

where N is the number of map iterations (an integer number of toroidal turns) before we stop the iteration in order to perform the above-mentioned procedure for locating the exact hitting point.

We investigate the distribution of connection lengths at the divertor plate for the two considered equilibria. For this we take 10^6 initial conditions at the plate $y = y_{H1}$ and whose horizontal coordinates are chosen to be close to the intersection of the ideal separatrix with the divertor plate $x_{sep} = 0.7071$. Each initial condition was iterated until it returns to the divertor plate. The lines depart from the divertor plate with positive values of x and strike the plate with negative values.

Figures 6(*a*) and 7(*a*) show the connection length distributions in terms of the field line displacement with respect to the divertor plate position $\Delta x = x_F - x_S$. Negative values of Δx correspond to positions in the external region and positive values to positions in the divertor private flux regions. The

peaks denote high connection lengths, amounting to field lines that stay in the plasma core for a comparatively large time. We observed that such field lines are near the stable invariant manifolds at the periphery of the chaotic region. Since these manifolds present complicated (in fact, fractal) striations we expect that the distribution of such peaks should present self-similarity. Indeed, a magnification of a region with large connection lengths shows a very complicated structure, which is present at all small scales of the distribution.

As a result of this self-similar character inherited from the fractal structure of the underlying chaotic saddle, the spatial distribution of field lines hitting the divertor plates is likewise fractal. We have obtained magnetic footprints, which are formed by the striking points of field lines at the divertor plate (ϕ_F, x_F), their final horizontal coordinate being always y_{H1}; these are depicted in figures 6(*b*) and 7(*b*). The magnetic footprints can be seen as marks on the divertor plate caused by escaping lines. The final horizontal positions are written in terms of the displacement Δx with respect to the left branch of the unperturbed separatrix intersection with the plate. For this figure, positive values of Δx correspond to final horizontal positions outside the unperturbed separatrix.

The connection length distributions are different for each equilibrium case, characterized by different values of the magnetic shear at the reference surface. The low-shear case ($\hat{s}_{95} = 1.8$) presents a region with high connection lengths that is smaller than the case of $\hat{s}_{95} = 2.67$. Both cases presents self-similarity in the distribution. This can be seen by observing the enlargement insets shown in figures 6(*a*) and 7(*a*). However, the latter case suggest a higher complexity in the fractal distribution. This means that two points very close at the plate can be reached by field lines with very different connection length values for $\hat{s}_{95}$. Moreover, the range of connection length values is larger for the high-shear considered. The consequence of this is a strongly nonuniform deposition pattern of energy and particles, as the magnetic shear at the edge increases.
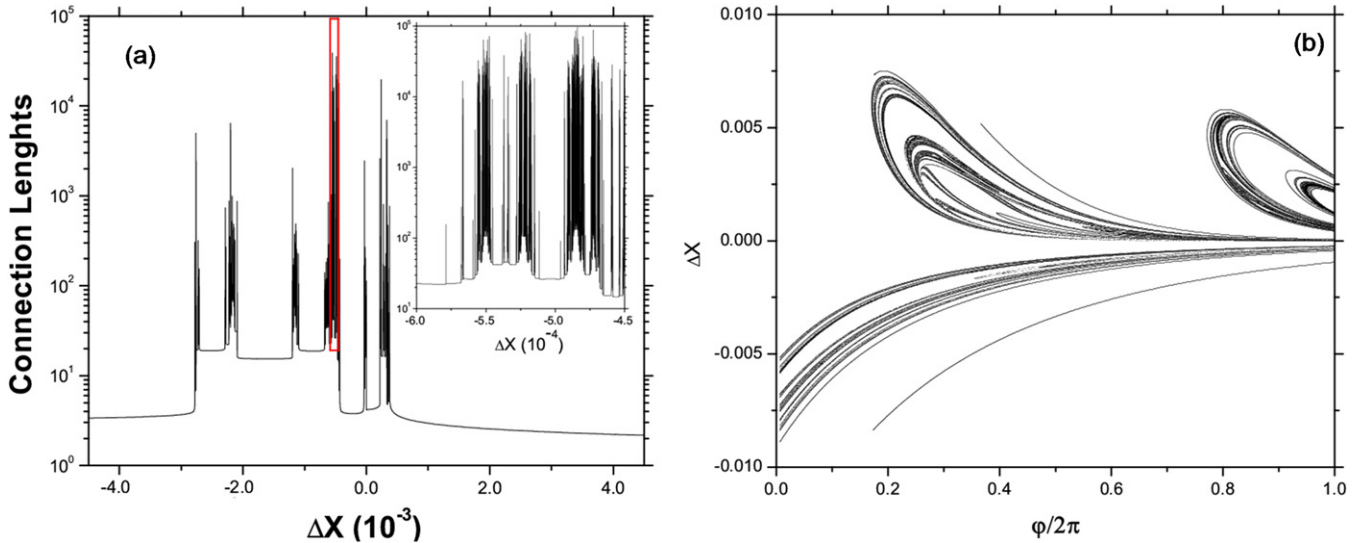
Figure 7. (*a*) Distribution of connection lengths of field lines colliding with the divertor plate for the same parameters as in figure 5(*b*). The inset shows a magnification of the box marked in red/gray. (*b*) Magnetic footprint corresponding to this case.

Figures 6(*b*) and 7(*b*) show the structure of magnetic footprints for the escape patterns whose connection length distributions were depicted in figures 6(*a*) and 7(*a*), respectively. The convoluted finger-like structures are similar to results previously obtained by Evans and collaborators through direct field line integration [34, 35]. The high-shear case $\hat{s}_{95} = 2.67$ of figure 7(*b*) has a larger deposition area for the field lines hitting the divertor plate, although with the same contours as the low-shear case $\hat{s}_{95} = 1.8$ of figure 6(*b*). The combined results of connection length distributions and magnetic footprint patterns indicate that high-shear equilibrium configurations provide a better deposition scenario than low-shear configurations, as far as the deposition area on the divertor plate is concerned.

If, in a lowest order approximation, particles follow the magnetic field lines until they reach the divertor plate, magnetic footprints would be related to the heat deposition pattern, which is experimentally accessible through bolometric measurements. As a matter of fact, recent laboratory studies reveal that the heat distribution pattern on divertor plates has some degree of self-similarity, thus confirming the fractal nature of magnetic footprints. Moreover, even in the presence of collisions, the fractal pattern of the escape channels persists, with some widening due to the random nature of the collisions [36].

5. Conclusions

The purpose of this paper was twofold. In the first place, we offered a further example of application of the trajectory integration method we previously used in a particular example in [22]. Both cases refer to single-null divertor tokamak configurations, i.e. both have a single x-point and an ideal separatrix separating the closed magnetic surfaces of the plasma core from the external surfaces. The latter surfaces are expected to be destroyed by symmetry-breaking perturbations, like those generated with an ergodic limiter, so as to yield a

chaotic field line region in the periphery. The divertor plate is conveniently placed within this chaotic region in such a way that escaping field lines from the chaotic region eventually hit the divertor and are collected.

A desirable feature of the example considered in this paper is that it can describe an equilibrium plasma model with a number of free parameters. This provides a high level of versatility for representing different magnetic geometries and safety factor profiles for application to different tokamaks. For example, the choice of safety factor profile is highly desirable since it provides the capability of varying the safety factor at the plasma edge and can simulate the effect of perturbations with different resonances. Moreover, by construction the maps obtained by the trajectory integration method are strictly symplectic, which is an important feature when performing long-time simulations, which are of importance, e.g. in transport studies.

In the second place, we have used the equilibrium model with the free parameters together with perturbation due to an ergodic limiter model to investigate the dependence of field line deposition patterns on the divertor plate with respect to different parameters describing magnetic shear at the plasma edge. The numerical diagnostics we have used were the distribution of the connection lengths (the time it takes for a field line to hit the divertor plate) and the magnetic footprints (the deposition pattern of field lines on the divertor plate). Both diagnostics suggest that high-sheared configurations produce wider deposition areas in the divertor plate, which may reflect better confinement properties, since the divertor aims to pump out escaping particles from the plasma before they reach the tokamak confinement vessel, where they can release impurities that contaminate the plasma core.

Appendix A. Explicit expression for the integrable divertor map

When a point is mapped from one point to another point in the same parabolic region, the complete set of map equations for the integrable divertor map is the following

- For $y_n < y_0$ and $K_1 < y_0$:

$$x_{n+1} = -(y_n - y_0)\sqrt{a_1}\sin(\sqrt{a_1}\Delta) + x_n\cos(\sqrt{a_1}\Delta), \tag{41}$$

$$y_{n+1} = (y_n - y_0)\cos(\sqrt{a_1}\Delta) + \frac{x_n}{\sqrt{a_1}}\sin(\sqrt{a_1}\Delta) + y_0. \tag{42}$$

- For $y_0 < y_n < y_{H1}$ and $y_0 < K_2 < y_{H1}$:

$$x_{n+1} = -(y_n - y_0)\sqrt{a_2}\sin(\sqrt{a_2}\Delta) + x_n\cos(\sqrt{a_2}\Delta), \tag{43}$$

$$y_{n+1} = (y_n - y_0)\cos(\sqrt{a_2}\Delta) + \frac{x_n}{\sqrt{a_2}}\sin(\sqrt{a_2}\Delta) + y_0. \tag{44}$$

- For $y_{H1} < y_n < y_S$ and $y_{H1} < K_3 < y_S$:

$$x_{n+1} = (y_n - y_S)\sqrt{a_3}\sinh(\sqrt{a_3}\Delta) + x_n\cosh(\sqrt{a_3}\Delta), \tag{45}$$

$$y_{n+1} = (y_n - y_S)\cosh(\sqrt{a_3}\Delta) + \frac{x_n}{\sqrt{a_3}}\sinh(\sqrt{a_3}\Delta) + y_S. \tag{46}$$

- For $y_S < y_n < y_{H2}$ and $y_S < K_4 < y_{H2}$:

$$x_{n+1} = (y_n - y_S)\sqrt{a_4}\sinh(\sqrt{a_4}\Delta) + x_n\cosh(\sqrt{a_4}\Delta), \tag{47}$$

$$y_{n+1} = (y_n - y_S)\cosh(\sqrt{a_4}\Delta) + \frac{x_n}{\sqrt{a_4}}\sinh(\sqrt{a_4}\Delta) + y_S. \tag{48}$$

- For $y_{H2} < y_n < 0$ and $y_{H2} < K_5 < 0$:

$$x_{n+1} = -y_n\sqrt{a_5}\sin(\sqrt{a_5}\Delta) + x_n\cos(\sqrt{a_5}\Delta), \tag{49}$$

$$y_{n+1} = y_n\cos(\sqrt{a_5}\Delta) + \frac{x_n}{\sqrt{a_5}}\sin(\sqrt{a_5}\Delta). \tag{50}$$

- For $y_n > 0$ and $K_6 > 0$:

$$x_{n+1} = -y_n\sqrt{a_6}\sin(\sqrt{a_6}\Delta) + x_n\cos(\sqrt{a_6}\Delta), \tag{51}$$

$$y_{n+1} = y_n\cos(\sqrt{a_6}\Delta) + \frac{x_n}{\sqrt{a_6}}\sin(\sqrt{a_6}\Delta). \tag{52}$$

When a point is mapped to a neighboring region we must use the transition equations, that are given as follows:

- For $y_n < y_0$ and $K_1 > y_0$:

$$x_{n+1} = y_0\cos(\sqrt{a_2}(\Delta - t_0)), \tag{53}$$

$$y_{n+1} = \frac{x_0}{\sqrt{a_2}}\sin(\sqrt{a_2}(\Delta - t_0)) + y_0, \tag{54}$$

where

$$x_0 = +\left[x_n^2 + a_1(y_n - y_0)^2\right]^{1/2}, \tag{55}$$

$$t_0 = \frac{1}{\sqrt{a_1}}\cos^{-1}\left[\frac{x_0 x_n}{x_n^2 + a_1(y_n - y_0)^2}\right]. \tag{56}$$

- For $y_0 < y_n < y_{H1}$ and $K_2 < y_0$:

$$x_{n+1} = x_0^*\cos(\sqrt{a_1}(\Delta - t_0^*)), \tag{57}$$

$$y_{n+1} = \frac{x_0^*}{\sqrt{a_1}}\sin(\sqrt{a_1}(\Delta - t_0^*)) + y_0. \tag{58}$$

where

$$x_0^* = -\left[x_n^2 + a_2(y_n - y_0)^2\right]^{1/2}, \tag{59}$$

$$t_0^* = \frac{1}{\sqrt{a_2}}\cos^{-1}\left[\frac{x_0^* x_n}{x_n^2 + a_2(y_n - y_0)^2}\right]. \tag{60}$$

- For $y_0 < y_n < y_{H1}$ and $K_2 > y_{H1}$:

$$\begin{aligned}x_{n+1} &= (y_{H1} - y_S)\sqrt{a_3}\sinh(\sqrt{a_3}(\Delta - t_{H1})) \\ &\quad + x_{H1}\cosh(\sqrt{a_3}(\Delta - t_{H1})),\end{aligned} \tag{61}$$

$$\begin{aligned}y_{n+1} &= (y_{H1} - y_S)\cosh(\sqrt{a_3}(\Delta - t_{H1})) \\ &\quad + \frac{x_{H1}}{\sqrt{a_3}}\sinh(\sqrt{a_3}(\Delta - t_{H1})) + y_S.\end{aligned} \tag{62}$$

where

$$\begin{aligned}x_{H1} &= +[x_n^2 + a_2(y_n - y_0)^2 + a_3(y_{H1} - y_S)^2 \\ &\quad + 2(b' - b)]^{1/2},\end{aligned} \tag{63}$$

$$t_{H1} = \frac{1}{\sqrt{a_2}}\cos^{-1}\left[\frac{x_{H1}x_n + a_2(y_{H1} - y_0)(y_n - y_0)}{x_n^2 + a_2(y_n - y_0)^2}\right]. \tag{64}$$

- For $y_{H1} < y_n < y_S$ and $K_3 < y_{H1}$

$$\begin{aligned}x_{n+1} &= -(y_{H1} - y_0)\sqrt{a_2}\sin(\sqrt{a_2}(\Delta - t_{H1}^*)) \\ &\quad + x_{H1}^*\cos(\sqrt{a_2}(\Delta - t_{H1}^*),\end{aligned} \tag{65}$$

$$\begin{aligned}y_{n+1} &= (y_{H1} - y_0)\cos(\sqrt{a_2}(\Delta - t_{H1}^*)) \\ &\quad + \frac{x_{H1}^*}{\sqrt{a_2}}\sin(\sqrt{a_2}(\Delta - t_{H1}^*) + y_0.\end{aligned} \tag{66}$$

where

$$\begin{aligned}x_{H1}^* &= -[x_n^2 - a_2(y_{H1} - y_0)^2 - a_3(y_n - y_S)^2 \\ &\quad + 2(b - b')]^{1/2},\end{aligned} \tag{67}$$

$$t_{H1}^* = \frac{1}{\sqrt{a_3}}\cosh^{-1}\left[\frac{x_{H1}^* x_n - a_3(y_n - y_S)(y_{H1} - x_S)}{x_n^2 - a_3(y_n - y_S)^2}\right]. \tag{68}$$

- For $y_{H1} < y_n < y_S$ and $K_3 > y_S$:

$$x_{n+1} = x_S\cosh(\sqrt{a_4}(\Delta - t_S)), \tag{69}$$

$$y_{n+1} = \frac{x_S}{\sqrt{a_4}}\sinh(\sqrt{a_4}(\Delta - t_S)) + y_S. \tag{70}$$

where

$$x_S = +\left[x_n^2 - a_3(y_n - y_S)^2\right]^{1/2}, \tag{71}$$

$$t_S = \frac{1}{\sqrt{a_3}}\cosh^{-1}\left[\frac{x_S x_n}{x_n^2 - a_3(y_n - y_S)^2}\right]. \tag{72}$$

- For $y_S < y_n < y_{H2}$ and $K_4 < y_S$:

$$x_{n+1} = x_S^*\cosh(\sqrt{a_3}(\Delta - t_S^*)), \tag{73}$$

$$y_{n+1} = \frac{x_S^*}{\sqrt{a_3}}\sinh(\sqrt{a_3}(\Delta - t_S^*)) + y_S. \tag{74}$$

where

$$x_S^* = -\left[x_n^2 - a_4(y_n - y_S)^2\right]^{1/2}, \tag{75}$$

$$t_S^* = \frac{1}{\sqrt{a_4}}\cosh^{-1}\left[\frac{x_S^* x_n}{x_n^2 - a_4(y_n - y_S)^2}\right]. \tag{76}$$

- For $y_S < y_n < y_{H2}$ and $K_4 > y_{H2}$:

$$x_{n+1} = -y_{H2}\sqrt{a_5}\sin(\sqrt{a_5}(\Delta - t_{H2}))$$
$$+ x_{H2}\cos(\sqrt{a_5}(\Delta - t_{H2})), \qquad (77)$$
$$y_{n+1} = y_{H2}\cos(\sqrt{a_5}(\Delta - t_{H2}))$$
$$+ \frac{x_{H2}}{\sqrt{a_5}}\sin(\sqrt{a_5}(\Delta - t_{H2})). \qquad (78)$$

where

$$x_{H2} = \left[x_n^2 - a_4(y_n - y_S)^2 - a_5 y_{H2}^2 + 2b\right]^{1/2}, \qquad (79)$$
$$t_{H2} = \frac{1}{\sqrt{a_4}}\cosh^{-1}\left[\frac{x_{H2}x_n - a_4(y_n - y_S)(y_{H2} - x_S)}{x_n^2 - a_4(y_n - y_S)^2}\right]. \qquad (80)$$

- For $y_{H2} < y_n < 0$ and $K_5 < y_{H2}$:

$$x_{n+1} = (y_{H2} - y_S)\sqrt{a_4}\sinh(\sqrt{a_4}(\Delta - t_{H2}^*))$$
$$+ x_{H2}^*\cosh(\sqrt{a_4}(\Delta - t_{H2}^*)), \qquad (81)$$
$$y_{n+1} = (y_{H2} - y_S)\cosh(\sqrt{a_4}(\Delta - t_{H2}^*))$$
$$+ \frac{x_{H2}^*}{\sqrt{a_4}}\sinh(\sqrt{a_4}(\Delta - t_{H2}^*)) + y_S. \qquad (82)$$

where

$$x_{H2}^* = -\left[x_n^2 + a_5 y_n^2 + a_4(y_{H2} - y_S)^2 - 2b\right]^{1/2}, \qquad (83)$$
$$t_{H2}^* = \frac{1}{\sqrt{a_5}}\cos^{-1}\left[\frac{x_{H2}^* x_n + a_5 y_n y_{H2}}{x_n^2 + a_5 y_n^2}\right]. \qquad (84)$$

- For $y_{H2} < y_n < 0$ and $K_5 > 0$:

$$x_{n+1} = x_C\cos(\sqrt{a_6}(\Delta - t_C)), \qquad (85)$$
$$y_{n+1} = \frac{x_C}{\sqrt{a_6}}\sin(\sqrt{a_6}(\Delta - t_C)). \qquad (86)$$

where

$$x_C = \left[x_n^2 + a_5 y_n^2\right]^{1/2}, \qquad (87)$$
$$t_C = \frac{1}{\sqrt{a_5}}\cos^{-1}\left[\frac{x_C x_n}{x_n^2 + a_5 y_n^2}\right]. \qquad (88)$$

- For $y_n > 0$ and $K_6 < 0$ 5:

$$x_{n+1} = x_C^*\cos(\sqrt{a_5}(\Delta - t_C^*)), \qquad (89)$$
$$y_{n+1} = \frac{x_C^*}{\sqrt{a_5}}\sin(\sqrt{a_5}(\Delta - t_C^*)). \qquad (90)$$

where

$$x_C^* = -\left[x_n^2 + a_6 y_n^2\right]^{1/2}, \qquad (91)$$
$$t_C^* = \frac{1}{\sqrt{a_6}}\cos^{-1}\left[\frac{x_C^* x_n}{x_n^2 + a_6 y_n^2}\right]. \qquad (92)$$

where we define the following quantities:

$$K_1 = (y_n - y_0)\cos(\sqrt{a_1}\Delta) + \frac{x_n}{\sqrt{a_1}}\sin(\sqrt{a_1}\Delta) + y_0, \qquad (93)$$
$$K_2 = (y_n - y_0)\cos(\sqrt{a_2}\Delta) + \frac{x_n}{\sqrt{a_2}}\sin(\sqrt{a_2}\Delta) + y_0, \qquad (94)$$
$$K_3 = (y_n - y_S)\cosh(\sqrt{a_3}\Delta) + \frac{x_n}{\sqrt{a_3}}\sinh(\sqrt{a_3}\Delta) + y_S, \qquad (95)$$

$$K_4 = (y_n - y_S)\cosh(\sqrt{a_4}\Delta) + \frac{x_n}{\sqrt{a_4}}\sinh(\sqrt{a_4}\Delta) + y_S, \qquad (96)$$
$$K_5 = y_n\cos(\sqrt{a_5}\Delta) + \frac{x_n}{\sqrt{a_5}}\sin(\sqrt{a_5}\Delta), \qquad (97)$$
$$K_6 = y_n\cos(\sqrt{a_6}\Delta) + \frac{x_n}{\sqrt{a_6}}\sin(\sqrt{a_6}\Delta). \qquad (98)$$

Appendix B. Natural rotation period of the magnetic surfaces

The integrable map accepts any choice of safety factor independently from the chosen geometry. To set a safety factor q for a specific surface $\Psi(x, y)$ we must use a value for the parameter Δ given by $\Delta = T/q$, where T is the natural rotation period of the surface $\Psi(x, y)$. In this appendix we give the expressions for $T(\Psi)$.

- For $y < y_S$ and $\Psi < [a_2(y_{H1} - y_0)^2/2 + b]'$ (entirely elliptic surfaces in the private flux region):

$$T = \pi\left[\frac{1}{\sqrt{a_1}} + \frac{1}{\sqrt{a_2}}\right], \qquad (99)$$

- For $y < y_S$ and $[a_2(y - y_0)^2/2 + b'] < \Psi < \Psi_S$ (surfaces with hyperbolic contribution in the private flux region):

$$T = \left[\frac{\pi}{\sqrt{a_1}} + \frac{2}{\sqrt{a_2}}\cos^{-1}\left(\frac{2\Psi - 2b' - a_2(y_{H1} - x_0)^2}{2\Psi - 2b'}\right)^{1/2}\right.$$
$$\left. + \frac{1}{a_3}\cosh^{-1}\left(\frac{\Psi + \Psi_S - a_2(y_{H1} - y_0)^2 - 2b'}{\Psi_S - \Psi}\right)\right], \qquad (100)$$

- For $y > y_S$ and $\Psi < a_5 y_{H2}^2/2$ (entirely elliptic surfaces in the plasma region):

$$T = \pi\left[\frac{1}{\sqrt{a_6}} + \frac{1}{\sqrt{a_5}}\right], \qquad (101)$$

- For $y > y_S$ and $a_5 y_{H2}^2/2 < \Psi < \Psi_S$ (surfaces with hyperbolic contribution in the plasma region):

$$T = \left[\frac{\pi}{\sqrt{a_6}} + \frac{2}{\sqrt{a_5}}\cos^{-1}\left(\frac{2\Psi - a_5 y_{H2}^2}{2\Psi}\right)^{1/2}\right.$$
$$\left. + \frac{1}{a_4}\cosh^{-1}\left(\frac{\Psi + \Psi_S - a_5 y_{H2}^2}{\Psi_S - \Psi}\right)\right], \qquad (102)$$

- For $\Psi > \Psi_S$ (surfaces external to the separatrix):

$$T = \left[\frac{\pi}{\sqrt{a_1}} + \frac{\pi}{\sqrt{a_6}}\right.$$
$$+ \frac{2}{\sqrt{a_2}}\cos^{-1}\left(\frac{2\Psi - 2b' - a_2(y_{H1} - y_0)^2}{2\Psi - 2b'}\right)^{1/2}$$
$$+ \frac{2}{\sqrt{a_5}}\cos^{-1}\left(\frac{2\Psi - a_5 y_{H2}^2}{2\Psi}\right)^{1/2}$$
$$+ \frac{2}{\sqrt{a_4}}\cosh^{-1}\left(\frac{2\Psi - a_5 y_{H2}^2}{2\Psi - 2\Psi_S}\right)^{1/2}$$
$$\left. + \frac{2}{\sqrt{a_3}}\cosh^{-1}\left(\frac{2\Psi - 2b' - a_2(y_{H1} - y_0)^2}{2\Psi - 2\Psi_S}\right)^{1/2}\right] \qquad (103)$$

References

[1] Boozer A 2005 *Rev. Mod. Phys.* **76** 1071
[2] Cordey J G, Goldston R J and Parker R R 1992 *Phys. Today* **45** 22
[3] Joseph I *et al* 2008 *Nucl. Fusion* **48** 045009
[4] Eich T, Herrmann A, Neuhauser J and ASDEX Upgrade Team 2003 *Phys. Rev. Lett.* **91** 195003
[5] Post D E and the ITER Team 1991 *ITER Documentation Series* No 21 (Vienna: IAEA)
[6] Casper T A *et al* 2008 *Fusion Eng. Des.* **83** 552
[7] Brix M 2008 *et al Rev. Sci. Instrum.* **79** 10F325
[8] Abdullaev S S and Finken K H 1998 *Nucl. Fusion* **38** 531
[9] Abdullaev S S *et al* 2006 *Nucl. Fusion* **46** S113
[10] Abdullaev S S 2009 *Phys. Plasmas* **16** 030701
[11] Abdullaev S S 2004 *Phys. Rev.* E **70** 046202
[12] Punjabi A and Verma A 1992 *Phys. Rev. Lett.* **69** 3322
[13] Punjabi A, Ali H and Boozer A 1997 *Phys. Plasmas* **4** 337
[14] Punjabi A, Ali H and Boozer A 2003 *Phys. Plasmas* **10** 3992
[15] Ali H *et al* 2004 *Phys. Plasmas* **11** 1908
[16] Barocio S R, Chávez-Alarcón E and Gutierrez-Tapi C 2006 *Braz. J. Phys.* **36** 550
[17] Punjabi A *et al* 2008 *Phys. Plasmas* **15** 082507
[18] Punjabi A and Ali H 2008 *Phys. Plasmas* **15** 122502
[19] Punjabi A and Ali H 2011 *Phys. Plasmas* **18** 022509
[20] Jones M *et al* 2009 *Phys. Plasmas* **16** 042511
[21] Punjabi A, Ali H and Farhat H 2009 *Plasma Phys. Control. Fusion* **51** 075009
[22] Kroetz T *et al* 2010 *Nucl. Fusion* **50** 034003
[23] Abbamonte P M and Morrison P J 1994 Constructing symplectic maps for application to magnetostatic and Hamiltonian mechanics *Institute for Fusion Studies Report IFSR* # 638 The University of Texas at Austin, Austin, TX
[24] Kinsey J E, Waltz R E and Candy J 2006 *Phys. Plasmas* **13** 022305
[25] Huysmans G T A 2005 *Plasma Phys. Control. Fusion* **47** 2107
[26] Huysmans G T A and Czarny O 2007 *Nucl. Fusion* **47** 659
[27] Pustovitov V D 2007 *Nucl. Fusion* **47** 563
[28] Park J *et al* 2008 *Nucl. Fusion* **48** 045006
[29] Jakubowski M W *et al* 2009 *Nucl. Fusion* **49** 095013
[30] Schmitz O *et al* 2008 *Plasma Phys. Control. Fusion* **50** 124029
[31] Vannucci A, Nascimento I C and Caldas I L 1989 *Plasma Phys. Control. Fusion* **31** 147
[32] Pires C J A *et al* 2005 *Plasma Phys. Control. Fusion* **47** 1609
[33] Martin T J and Taylor J B 1984 *Plasma Phys. Control. Fusion* **26** 321
[34] Wingen A, Evans T E and Spatschek K H 2009 *Nucl. Fusion* **49** 055027
[35] Wingen A, Evans T E and Spatschek K H 2009 *Phys. Plasmas* **16** 042504
[36] Schelin A B, Caldas I L, Viana R L and Benkadda M 2011 *Phys. Lett.* A **376** 24
[37] Morrison P J 2000 *Phys. Plasmas* **7** 2279
[38] Caldas I L *et al* 1996 *Chaos Solitons Fractals* **7** 991
[39] Kroetz T *et al* 2008 *Phys. Plasmas* **15** 092310
[40] Viana R L *et al* 2011 *Phil. Trans. R. Soc. Lond.* A **369** 371